RESEARCH ARTICLE

Check for updates

Structural reconstruction of BiPbO₂Br nanosheets for electrochemical CO₂ reduction to formate†

Gaoming Sun,‡[ab] Chong Zou,‡[c] Wen Sun, [ID][ab] Ying Fang,[ab] Shuijian He, [ID][d] Yana Liu,[ab] Jiguang Zhang, [ID][ab] Yunfeng Zhu [ID]*[ab] and Jun Wang [ID]*[ab]

The electrochemical reduction of CO_2 to value-added products represents a promising strategy to store renewable energy and realize global carbon neutrality. Bi-based materials have attracted extensive attention for formate production from CO_2 reduction. Herein, we employ BiPbO₂Br nanosheets as the bimetallic oxyhalide precursor to prepare a reconstructed Bi–Pb composite catalyst by electroreduction. The resultant catalyst exhibits impressive performance for formate production, including a high partial current density (40 mA cm⁻² at −1.0 V), a high faradaic efficiency (96.6% at −0.9 V), a high energy conversion efficiency (>50% from −0.8 to −1.1 V), and good stability. As compared with the monometallic Bi and Pb counterparts, the Bi–Pb composite catalyst demonstrates superior intrinsic performance, which is attributed to the multiphase composites and abundant heterogeneous interfaces derived from electroreduction induced structural reconstruction of BiPbO₂Br. This work offers an attractive strategy to further improve the performance of Bi catalysts for CO_2 reduction to formate.

1. Introduction

The worldwide energy demand is largely covered by fossil fuels, which brings about massive carbon dioxide (CO_2) emission in the atmosphere, resulting in the ever-growing global warming and environmental load.[1–3] The electrochemical CO_2 reduction reaction (CO_2RR) using sustainable energies provides a promising strategy for not only recycling CO_2 into valuable chemicals or liquid fuels, but also storing electricity from renewable energy sources such as solar and wind.[4,5] Over the past decade, it has been demonstrated that the CO_2RR can undergo multiple proton-coupled electron transfer processes, leading to the formation of diversified products such as carbon monoxide (CO), formic acid (HCOOH), methane (CH_4), ethylene (C_2H_4), methanol (CH_3OH), ethanol (C_2H_5OH), and so on.[6–9] Among them, regarding the energy input and market price of the product, the CO_2RR to formic acid (or formate) is more economically

profitable.[10–12] Besides, formate is widely used in the chemical industry as a raw material, as well as energy sectors as a liquid hydrogen storage carrier or a high energy density fuel.[13–15] Given these, the scientific community has put a lot of efforts to explore efficient electrocatalysts for selective formate production *via* the CO_2RR.

So far, numerous metallic catalysts, such as Pd, Bi, In, Pb, and Sn, have shown the capability to electrochemically convert CO_2 to formate.[16–18] As per the reported results, Bi-based catalysts stand out due to the weak affinity to key *OCHO intermediates and poor activity for the undesired hydrogen evolution reaction (HER), enabling high faradaic efficiency (FE) for formate production.[19–22] To meet the requirements of practical application, however, it is still imperative to explore effective strategies to optimize the performance of Bi electrocatalysts, that is, achieving large formate partial current density ($j_{formate}$) at low overpotential. Morphology engineering has been proved to be one of the effective means, which can be achieved using nanostructured Bi-based compounds (such as oxides, sulfides, and oxyhalides) through *in situ* electroreduction.[23–31] Beyond this, the introduction of another element to form a Bi-containing binary component may create multiphase composites and heterogeneous interfaces during the electroreduction induced structural reconstruction, which is expected to regulate the active sites and optimize the adsorption and stabilization of the reaction intermediates. As a result, recent studies on binary composite catalysts, such as Bi–Cu, Bi–Sn, Bi–Ag, Bi–Ce, and so on,[32–38] have demonstrated favorable formate production. Besides, Pb doped Zn or Cu can also facilitate the CO_2RR to

[a] College of Materials Science and Engineering, Nanjing Tech University, 30 South Puzhu Road, Nanjing 211816, China. E-mail: jun22@njtech.edu.cn, yfzhu@njtech.edu.cn

[b] Jiangsu Collaborative Innovation Centre for Advanced Inorganic Function Composites, Nanjing Tech University, Nanjing 211816, China

[c] School of Chemistry and Molecular Engineering, Nanjing Tech University, Nanjing 211816, China

[d] Co-Innovation Centre of Efficient Processing and Utilization of Forest Resources, College of Materials Science and Engineering, Nanjing Forestry University, Nanjing 210037, China

‡ These authors contributed equally to this work.

formate with impressive performance.[39,40] Nevertheless, the combination of Bi and Pb has been rarely reported for the CO₂RR.

Bearing these aspects in mind, therefore, we herein employ BiPbO₂Br nanosheets (NSs) as the bimetallic oxyhalide precursor to prepare a reconstructed Bi–Pb composite catalyst *via* electroreduction. When evaluated in an H-type reaction cell, the resultant catalyst exhibits high activity and selectivity towards formate production. The $j_{formate}$ reaches up to 40 mA cm^{-2} at -1.0 V *versus* the reversible hydrogen electrode (RHE) with an FE of 93.1%. The catalyst also achieves impressive energy efficiency (EE) over a wide potential window and good long-term stability. Compared with monometallic Bi and Pb counterparts, the Bi–Pb catalyst demonstrates superior intrinsic performance for the CO₂RR to formate, which is associated with the abundant heterogeneous interfaces created by electroreduction induced structural reconstruction.

2. Experimental section

2.1. Chemicals and materials

All the chemical reagents, including bismuth nitrate pentahydrate (Bi(NO₃)₃·5H₂O, Aladdin, AR, ≥99%), lead acetate trihydrate (C₂H₄O₃Pb·3H₂O, Sinopharm, AR, ≥99.5%), hexadecyl trimethyl ammonium bromide (CTAB, Macklin, ≥99%), ethanol (Macklin, AR, ≥99.7%), sodium bromide (NaBr, Macklin, AR, ≥99%), mannitol (Aladdin, HPLC, ≥99%), ammonium hydroxide solution (NH₃·H₂O, Macklin, ≥28% NH₃ in H₂O), sodium carbonate (Na₂CO₃, Aladdin, 99.99%), sodium formate (Aladdin, 99.99%), deuterium oxide (D₂O, Macklin, 99.9% D), dimethyl sulfoxide (DMSO, Aladdin, ≥99.9%), Nafion proton exchange membrane (N117, Dupont), Nafion solution (5 wt% in ethanol, Dupont), Vulcan XC-72 C (Cabot), carbon paper (TORAY), CO₂ gas (99.999%) and Ar gas (99.99%), were used as purchased without further purification. Deionized water was used in all experiments with a specific resistance of 18.2 MΩ cm.

2.2. Synthesis of BiPbO₂Br NSs

The BiPbO₂Br NSs were synthesized following a previously reported method.[41] Briefly, 0.5 mmol of CTAB was added into 20 mL of ethanol containing Bi(NO₃)₃·5H₂O (0.5 mmol) and C₂H₄O₃Pb·3H₂O (0.5 mmol), which was continuously stirred until complete dissolution. After adding 5 ml of NH₃·H₂O and stirring for 1 h, the mixture solution was transferred into a 50 ml Teflon-lined stainless autoclave and heated at 190 °C for 12 h. Followed by cooling to room temperature, light yellow precipitates were collected by filtration and washing with water and ethanol and freeze-dried to obtain BiPbO₂Br NSs.

2.3. Synthesis of BiOBr NSs

In a typical synthesis of BiOBr NSs,[42] 1.5 mmol of Bi(NO₃)₃·5H₂O was dissolved in 30 ml of 0.1 M mannitol solution with stirring to obtain a transparent solution. After that, 1.5 mmol of NaBr was added into the above solution. The mixture solution was stirred for 0.5 h and then transferred into a

50 ml Teflon-lined stainless autoclave and heated at 160 °C for 3 h. After cooling to room temperature, white precipitates were collected by filtration and washing with water and ethanol and freeze-dried to obtain BiOBr NSs.

2.4. Synthesis of PbOₓBrᵧ

The PbOₓBrᵧ was synthesized using a similar procedure to that of BiPbO₂Br without the addition of Bi(NO₃)₃·5H₂O.

2.5. Characterization

The crystalline structure of the samples was analyzed by X-ray diffraction (XRD) using an ARL-X'TRA diffractometer with Cu Kα radiation (40 kV and 35 mA). Field emission scanning electron microscopy (FE-SEM) was performed to detect the morphology of the samples by using JSM-5900. Transmission electron microscopy (TEM), selected area electron diffraction (SAED), and energy-dispersive X-ray spectroscopy (EDS) were performed with an FEI Talos F200X G2 electron microscope. X-Ray photoelectron spectroscopy (XPS) was performed using a Thermo Fisher Scientific ESCALAB 250Xi with 200 W monochromated Al Kα radiation. Raman spectra were recorded on LabRAM HR Evolution with a diode laser emitting 532 nm.

2.6. Preparation of the working electrode

The catalyst loaded onto carbon paper (1 × 1 cm²) was used as the working electrode. The catalyst ink was prepared by dispersing 8.3 mg of the as-prepared catalyst and 2.8 mg of XC-72 C in a mixture of 1.2 mL of ethanol and 0.4 mL of H₂O, and then 35 μL of Nafion was added and sonicated for 2 h to produce a homogenous suspension. Afterwards, the catalyst ink was airbrushed on to carbon paper and dried in air at room temperature. The total loading on carbon paper was controlled to be 1 mg cm^{-2}, indicating the effective catalyst loading of 0.75 mg cm^{-2}.

2.7. Electrochemical measurements

All the electrochemical measurements were performed using a CHI660E potentiostat, with a gas-tight two-compartment H-type electrochemical cell separated by a piece of Nafion 117 membrane. A piece of Pt gauze and Ag/AgCl/sat. KCl were used as the counter electrode and reference electrode, respectively. The electrolyte, 0.5 M NaHCO₃ (pH = 7.3), was prepared by purging CO₂ into 0.25 M Na₂CO₃ aqueous solution. Linear sweep voltammetry (LSV) was performed at a rate of 10 mV s^{-1}. The CO₂RR activity of the electrode was evaluated in a CO₂-saturated electrolyte using controlled potential electrolysis for 1 h at room temperature. During each electrolysis, the electrolyte was continuously bubbled with CO₂ at a flow rate of 10 sccm. All potentials were 85% iR-compensated and converted to RHE scale *via* the equation: $E_{RHE} = E_{Ag/AgCl} + 0.0591 \times pH + 0.197$ V. The reported current density was normalized to the geometric surface area of the carbon paper electrode unless otherwise specified.

2.8. Product analysis

The gas products, such as CO and H₂, were analyzed by online gas chromatography (GC, 9790Plus, Zhejiang Fuli) with Ar as

the carrier gas. The liquid product was determined by ^{1}H nuclear magnetic resonance (^{1}H NMR, Bruker Avance III 400 MHz) with the water suppression method. The NMR sample was prepared by mixing 0.5 mL of electrolyte after electrolysis with 0.1 mL of D_2O. To quantify the yield of formate in the electrolyte, a calibration curve was built using standard sodium formate solution with a known concentration (Fig. S1, ESI†).

2.9. Calculations

The FE of formate was calculated based on the charge consumed for formate production and the total charge passed through the electrode:

$$FE = \frac{A}{S} \times \frac{VnF}{Q}$$

in which A is the ^{1}H NMR peak area of formate, S is the coefficient ($10\,014.18\ mM^{-1}$) of the calibration curve in Fig. S1 (ESI†), V is the volume (25 mL) of the electrolyte in the cathodic compartment, n is the number of electrons transferred per formate ($n = 2$), F is the Faraday constant ($96\,485\ C\ mol^{-1}$), and Q is the total charge consumed during the electrolysis.

The electrochemical active surface area (ECSA) was determined by the following equation:

$$ECSA = \frac{C_{dl}}{C_s}S$$

in which S is the geometric area of the work electrode ($1\ cm^2$), C_{dl} is the double-layer capacitance, and C_s is the specific capacitance ($40\ \mu F\ cm^{-2}$).[33,38]

The EE for the CO_2RR to formate was estimated according to the following equation:[34]

$$EE = \frac{\left(1.23 - E_{eq,formate}\right)FE}{\left(1.23 - E_{eq,formate}\right) + \eta_{cathode}}$$

where 1.23 V is the thermodynamic equilibrium potential for the anode OER reaction, $E_{eq,formate}$ is the thermodynamic equilibrium potential for the cathode reaction to formate ($E_{eq,formate} = -0.03$ V), and $\eta_{cathode}$ is the cathode overpotential.

3. Results and discussion

The synthesis of $BiPbO_2Br$ NSs were achieved *via* a one-step hydrothermal method, as depicted in Scheme 1. Briefly, the metallic precursors of lead acetate and bismuth nitrate were stoichiometrically mixed with an aqueous solution containing ammonium hydroxide and CTAB in a Teflon-lined stainless autoclave, followed by hydrothermal treatment. Of note, CTAB
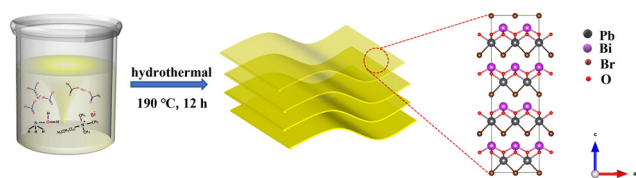
possesses a dual functionality of both the surfactant and the bromine source. The monometallic BiOBr and PbO_xBr_y were also synthesized and used for control experiments.

The crystal structure of the as-prepared samples was first investigated by XRD. As shown in Fig. S2 (ESI†), the XRD pattern of BiOBr NSs well matches with the layered tetragonal matlockite structure (PDF# 09-0393), which is alternatively composed of the $[Bi_2O_2]^{2+}$ layer and Br^- ion layer.[43] After the introduction of Pb^{2+}, the $BiPbO_2Br$ NSs still show an isostructure of the tetragonal phase BiOBr, wherein the Bi^{3+} in the pristine $[Bi_2O_2]^{2+}$ layer is randomly substituted with Pb^{2+} with a Bi/Pb molar ratio of 1. Fig. 1(a) shows that the XRD pattern of the sample can be readily indexed to tetragonal $BiPbO_2Br$ (PDF# 38-1008). Specifically, the observed $(00l)$ peak in the 2θ range of $<20°$ indicates an ordered stacking along the c-axis.[44–46] TEM images (Fig. 1(b) and (c)) show the irregular sheet-like morphology of $BiPbO_2Br$ with the lateral size ranging from tens to hundreds of nanometers and the average thickness of around 18 nm. As shown in Fig. 1(d), the layered stacking feature can be clearly identified from the high-resolution TEM (HRTEM) image, in which the lattice fringe distance is measured to be 0.642 nm, corresponding to the (002) plane of the tetragonal $BiPbO_2Br$. Further analysis of the surface of $BiPbO_2Br$ NSs (Fig. 1(e)) also reveals the (103) plane with a lattice spacing of 0.291 nm. Besides, the SAED pattern shows the (103), (211) and (109) planes of $BiPbO_2Br$ (Fig. 1(f)), consistent with the XRD results. Moreover, the high-angle annular dark-field scanning TEM (HAADF-STEM) and the corresponding EDS element mapping images (Fig. 1(g)–(k)) confirm the homogenous distribution of Bi, Pb, O and Br elements over $BiPbO_2Br$ NSs. Comparatively, the as-prepared tetragonal phase BiOBr is
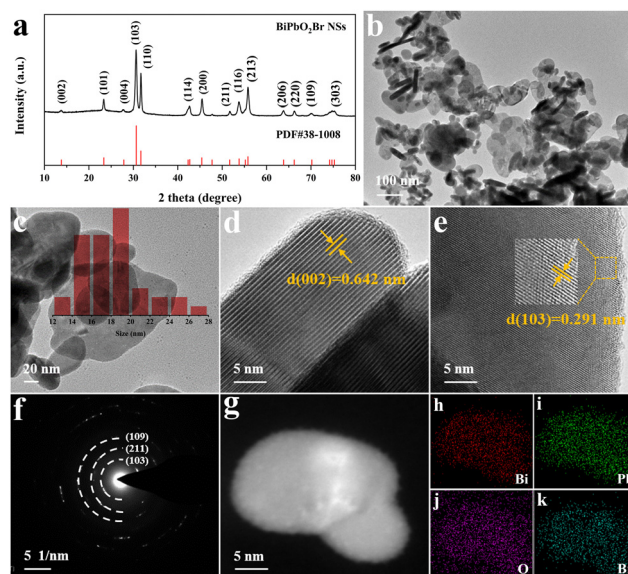

Fig. 1 Structural characterization of $BiPbO_2Br$ NSs. XRD pattern (a), TEM (b) (c) and HRTEM (d) and (e) images of $BiPbO_2Br$ NSs. Inset (c): The thickness distribution. (f) Shows the SAED pattern. (g) HAADF-STEM image and the (h)–(k) corresponding EDS elemental mapping of Bi, Pb, O, Br in $BiPbO_2Br$ NSs.
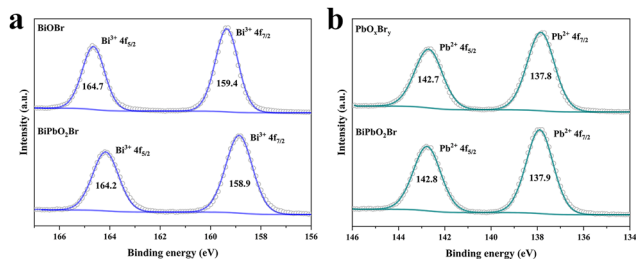

Scheme 1 Schematic illustration of the synthesis of $BiPbO_2Br$ NSs.

This journal is © The Royal Society of Chemistry and the Chinese Chemical Society 2023

Fig. 2 (a) Bi 4f XPS spectra of $BiPbO_2Br$ and BiOBr. (b) Pb 4f XPS spectra of $BiPbO_2Br$ and PbO_xBr_y.

Fig. 3 (a) LSV curves of $BiPbO_2Br$, BiOBr, and PbO_xBr_y in CO_2- or Ar-saturated 0.5 M $NaHCO_3$ with a scanning rate of 10 mV s^{-1}. (b) FE and (c) $j_{formate}$ in CO_2-saturated 0.5 M $NaHCO_3$ at various potentials over $BiPbO_2Br$, BiOBr, and PbO_xBr_y. (d) Long-term chronoamperometric test and the corresponding FE of $BiPbO_2Br$ at −0.9 V in CO_2-saturated 0.5 M $NaHCO_3$. Error bars denote the standard deviation of data from three tests.

in a quasi-square sheet morphology (Fig. S3, ESI†), in agreement with the previous report.[42] Similar to PbO_xBr_y, it mainly exists as biphasic bulk particles composed of $Pb_8O_7Br_2$ and $Pb_4O_3Br_2$ (Fig. S4 and S5, ESI†).

To discover the chemical state, XPS measurements were performed on the as-prepared samples. The survey spectrum verifies the existence of Bi, Pb, O and Br elements on the surface of $BiPbO_2Br$ (Fig. S6, ESI†). In the high resolution XPS spectra of Bi 4f (Fig. 2(a)), the binding energies of 158.9 and 164.2 eV are observed for $BiPbO_2Br$, corresponding to $4f_{7/2}$ and $4f_{5/2}$ of Bi^{3+}, which are lower than those for BiOBr. In contrast, two Pb 4f peaks of $BiPbO_2Br$ at 137.9 and 142.8 eV shift to higher energies compared to those of PbO_xBr_y (Fig. 2(b)). These observations suggest the electron flow from Pb to Bi in $BiPbO_2Br$, which could be ascribed to the smaller ionic radius of Bi^{3+} together with the structural distortion induced by Pb introduction.[46] Undoubtedly, the results mentioned above evidence the successful synthesis of $BiPbO_2Br$ NSs in this work.

To evaluate the CO_2RR performance, the catalytic reactions were investigated in a gas-tight H-type reaction cell using 0.5 M $NaHCO_3$ as the electrolyte. The obtained $BiPbO_2Br$, BiOBr and PbO_xBr_y were mixed with conductive carbon and spray-coated on a carbon paper electrode, which were then electrochemically reduced at −0.9 V before the measurements. The catalytic activities were first examined by linear sweep voltammetry (LSV). As shown in Fig. 3(a), the cathodic current density of $BiPbO_2Br$ in the Ar-saturated electrolyte is quite low, which mostly originates from the HER. However, when the electrolyte is saturated with CO_2, the current density dramatically increases below −0.6 V and approaches −77.5 mA cm^{-2} at −1.2 V, suggesting the substantial activity of $BiPbO_2Br$ for the CO_2RR. Comparatively, a much lower current density of PbO_xBr_y indicates its unfavorable CO_2RR activity, while BiOBr shows a slightly higher current density than $BiPbO_2Br$ in the same potential region, which could be contributed by its higher surface area and HER partial activity (vide infra). To systematically investigate the product distribution from the CO_2RR, the controlled electrolysis at different cathodic potentials was performed on the three catalytic electrodes (Fig. S7, ESI†). The gaseous and liquid products were separately quantified using online gas chromatography (GC) and nuclear magnetic resonance (NMR) spectroscopy, respectively. It is found that formate is the exclusive liquid product generated over $BiPbO_2Br$ throughout all potentials, together with a small amount of gaseous products including H_2
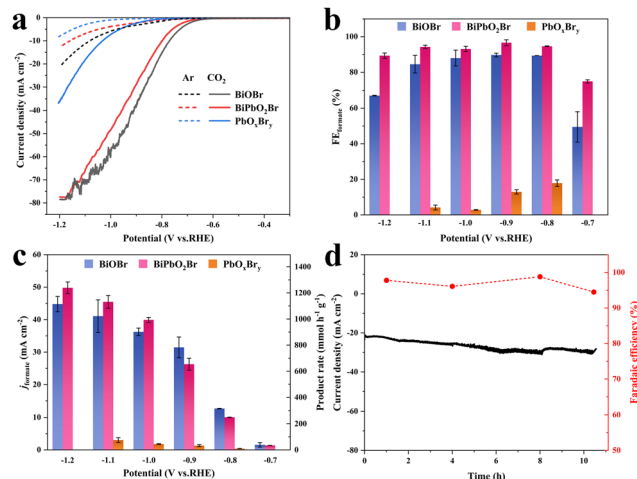
and CO (Fig. 3(b) and Fig. S8, S9, ESI†). At the initial potential (−0.7 V), the CO_2RR does not prevail over the HER completely due to its higher activation barrier and inferior reaction kinetics, resulting in the formate FE of 74.9%. Nevertheless, the FEs are increased and maintained at more than 90% across a wide potential region from −0.8 to −1.1 V, with the maximum of 96.6% obtained at −0.9 V. As the potential shifts to a more negative value (−1.2 V), the FE of formate reduces to 89.3%, which may suffer from CO_2 mass-transport limitation in the aqueous electrolyte and H-type reaction cell.[32] For the control sample of BiOBr, a similar tendency on the potential-dependent formate FE is observed. Although the formate generation dominated in the product distribution, the obtained FEs of BiOBr are lower than those of $BiPbO_2Br$ over all measured potentials. Besides, different from $BiPbO_2Br$ and BiOBr, PbO_xBr_y shows a much more favorable selectivity for the HER, exhibiting the highest formate FEs of <20%. These comparisons demonstrate that the Bi catalyst possesses high selectivity for electrochemical conversion of CO_2 to formate, while Pb introduction is facilitated for the further suppression of the competitive HER.

Furthermore, the according $j_{formate}$ and production rate of formate are calculated as shown in Fig. 3(c). Apparently, the $j_{formate}$ is found to increase gradually with the increase of overpotential for both $BiPbO_2Br$ and BiOBr. It is observed that $BiPbO_2Br$ exhibits lower $j_{formate}$ as compared to BiOBr in the low potential region (−0.7 to −0.9 V), which is largely due to its inferior total current density (Fig. S7, ESI†). However, this trend is totally reversed in the high potential region (−1.0 to −1.2 V), attributing to the reduced difference of the total current density and the superior formate FE (Fig. 3(b)). Typically, the $j_{formate}$ and formate production rate can reach up to 26 mA cm^{-2} (FE of 96.6%) and 654 mmol h^{-1} g^{-1} at −0.9 V over $BiPbO_2Br$, which are further increased to 40 mA cm^{-2} (FE of 93.1%) and 993 mmol h^{-1} g^{-1} at −1.0 V. From the perspective of practical

application, achieving more formate production at a large overpotential is highly desired, highlighting the critical role of Pb in $BiPbO_2Br$. Regarding PbO_xBr_y, the combination of the inferior total current density and formate FE results in the negligible $j_{formate}$. Of note, negligible formate is produced when using the Ar-saturated electrolyte instead, confirming the formate production exclusively from the electroreduction of CO_2 input (Fig. S10, ESI†). Finally, the stability of $BiPbO_2Br$ was accessed through a long-term electrolysis at −0.9 V. As shown in Fig. 3(d), the current density gradually increases from 21 to 30.5 mA cm^{-2} after more than 10 h of electrolysis, which is mainly ascribed to the decreased contact resistance of the electrode during the dynamic structural evolution of the catalyst for the CO_2RR (Fig. S11, ESI†). Nevertheless, high formate FEs of approximately 95% are still maintained at different sampling time intervals. It should be noted that the superior activity and selectivity of $BiPbO_2Br$ toward formate production for the CO_2RR are comparable or even better than those of many materials ever measured in an H-type cell (Table S1, ESI†).

To figure out if the activities of $BiPbO_2Br$ and $BiOBr$ were dependent on their ECSAs, the C_{dl} was determined by cyclic voltammetry measurement (Fig. S12, ESI†). Fig. 4(a) reveals that $BiOBr$ possesses larger C_{dl} and thus ECSA than $BiPbO_2Br$, which exactly explains their difference in current density (Fig. 3(a) and Fig. S7, ESI†). Subsequently, to reflect the intrinsic activity, the $j_{formate}$ is normalized with respect to the calculated ECSA of $BiPbO_2Br$ (75.75 cm^2) and $BiOBr$ (102.25 cm^2). As shown in Fig. 4(b), $BiPbO_2Br$ exhibits higher normalized current density than $BiOBr$ throughout all potentials, indicating its intrinsically superior activity for selective conversion of CO_2 to formate. Besides, the Tafel slope of $BiPbO_2Br$ is measured to be 92 mV dec^{-1}, smaller than the value of 99 mV dec^{-1} for $BiOBr$ (Fig. 4(c)), verifying that the presence of Pb is favorable for improving the reaction kinetics of formate production. Moreover, EE is another essential metric of the electrocatalyst for the practical application of the CO_2RR. Benefiting from

the combination of high FE and low overpotential for formate production, $BiPbO_2Br$ shows a high EE of over 50% in a wide potential region ranging from −0.8 to −1.1 V, with the maximum value of 58.7% obtained at −0.8 V (Fig. 4(d)).

It can be expected that the electroreduction process of the catalyst will give rise to the evolution of structure and chemical states, forming a self-regulation state, which has a significant influence on the exhibited performance for the CO_2RR.[32–38] To unveil the origin of the superior performance, the self-regulation state of $BiPbO_2Br$ was analyzed after electroreduction (denoted as R-$BiPbO_2Br$). First, the time dependent structural reconstruction is validated by XRD (Fig. 5(a)). Obviously, the electroreduction leads to a gradual disappearance of $BiPbO_2Br$ peaks, and the emergence of diffraction peaks of metallic Bi, $Bi_2O_2CO_3$, and $PbCO_3$. Due to the high oxophilicity, metallic Bi shows a relatively weak diffraction signal, readily forming $Bi_2O_2CO_3$ in the bicarbonate electrolyte.[20] Additionally, the absence of metallic Pb signals may be attributed to the occurrence of the spontaneous galvanic replacement reaction and primary cell reaction given the difference of redox potential between Pb ($E^\theta_{Pb^{2+}/Pb} = -0.126$ V $vs.$ SHE) and Bi ($E^\theta_{Bi^{3+}/Bi} = +0.308$ V $vs.$ SHE). This assumption can be indirectly affirmed by the observation of metallic Bi and Pb signals from monometallic $BiOBr$ and PbO_xBr_y after electroreduction,
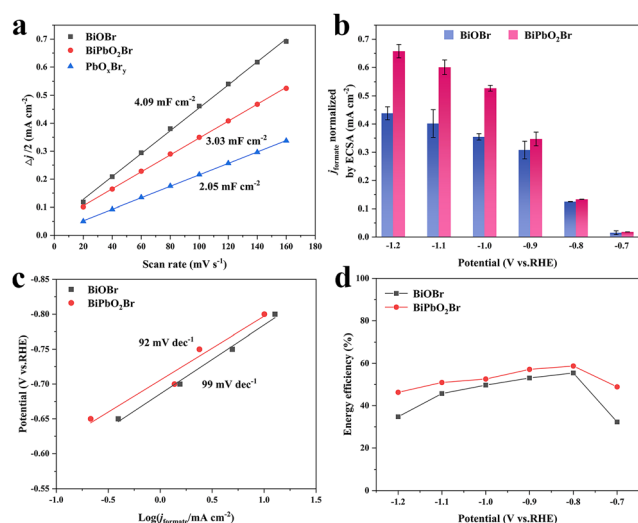
Fig. 4 (a) Charging current density plotted against scan rates on $BiPbO_2Br$, $BiOBr$, and PbO_xBr_y for estimating C_{dl} and ECSA. (b) ECSA normalized $j_{formate}$, (c) Tafel slope, and (d) EE of $BiPbO_2Br$ and $BiOBr$.
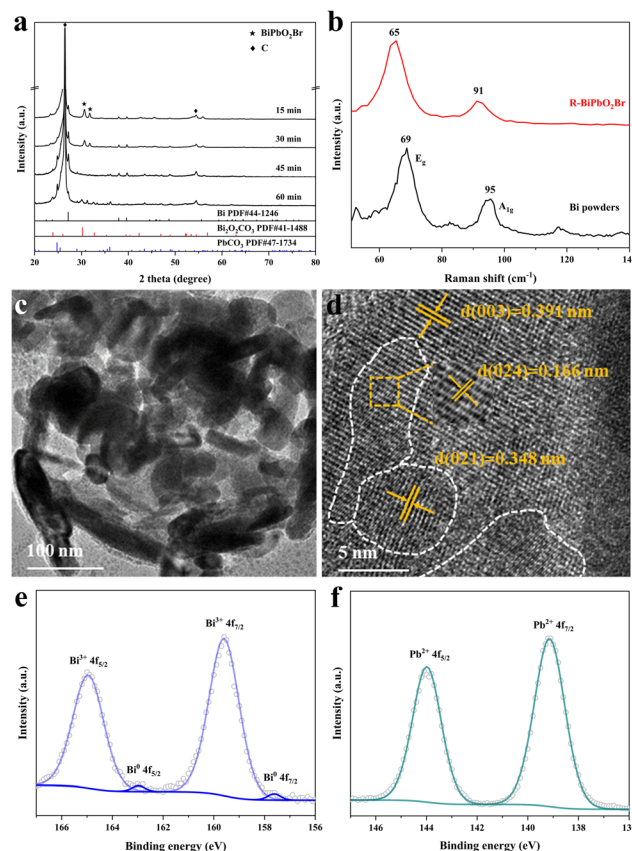
Fig. 5 (a) XRD pattern of R-$BiPbO_2Br$ with different reduction times. (b) Raman spectra of R-$BiPbO_2Br$ and Bi powders. (c) TEM and (d) HRTEM images of R-$BiPbO_2Br$. (e) Bi 4f and (f) Pb 4f XPS spectra of R-$BiPbO_2Br$.

respectively (Fig. S13, ESI†). Fig. 5(b) reveals the Raman spectrum of R-BiPbO$_2$Br, and the observed peaks at 65 and 91 cm^{-1} are ascribed to the E$_g$ and A$_{1g}$ bands of metallic Bi. In contrast to Bi powders, the Raman blue shift of R-BiPbO$_2$Br may be due to the decreased grain size.[47] Subsequently, TEM measurements reveal that R-BiPbO$_2$Br well inherits its pristine nanosheet-like morphology (Fig. 5(c)). From the HRTEM image, the lattice fringe distances of 0.391, 0.166, 0.348 nm are identified in different areas (Fig. 5(d)), which can be assigned to the planes of Bi (003), Bi$_2$O$_2$CO$_3$ (024), and PbCO$_3$ (021), respectively, indicating the formation of heterogeneous interfaces. The XPS measurements show free bromine on the surface of R-BiPbO$_2$Br (Fig. S14, ESI†), confirming the complete structural reconstruction during electroreduction. The presence of a small amount of metallic Bi in addition to Bi^{3+} and Pb^{2+} is also observed (Fig. 5(e) and (f)), in agreement with the XRD and TEM results.

Previous studies have demonstrated that the conversion of CO$_2$ to formate on Bi generally adopts an *OCHO intermediate pathway with oxygen atom binding to the Bi sites.[19–22] The construction of heterogeneous interfaces will promote the electron delocalization of interfacial Bi sites, facilitating the strong interaction with the *OCHO intermediate and thereby the production of formate.[33–38] In this work, therefore, the presence of Pb in BiPbO$_2$Br is beneficial for forming and stabilizing the multiphase composites during the structural reconstruction induced by electroreduction, thus facilitating the formation of abundant heterogeneous interfaces, which play the critical role in enhancing the activity and selectivity of interfacial Bi sites for the CO$_2$RR to formate.

4. Conclusions

In summary, we have developed a Bi–Pb composite catalyst through the electroreduction of BiPbO$_2$Br nanosheets for the CO$_2$RR, which exhibits impressive performance for formate production, including a high activity ($j_{formate}$ of 40 mA cm^{-2} at -1.0 V), a high selectivity (FE of 96.6% at -0.9 V), and a high energy conversion efficiency (EE of >50% from -0.8 to -1.1 V). The catalyst also shows good stability with no degradation of current density and a formate FE of around 95% is maintained over 10 h. More importantly, the Bi–Pb composite catalyst demonstrates superior intrinsic performance for the CO$_2$RR to formate, as compared with its monometallic Bi and Pb counterparts. The detailed investigation indicates that the structural reconstruction of BiPbO$_2$Br during electroreduction is favorable for the formation and stabilization of the multiphase composites, creating abundant heterogeneous interfaces and thus enhancing the intrinsic performance. This work highlights the role of Pb introduction in promoting the Bi catalyst for the CO$_2$RR to formate, which may offer guidance for the rational design of other efficient bimetallic catalysts with heterogeneous interfaces.

Author contributions

G. Sun, C. Zou, Y. Zhu, and J. Wang conceived the project. G. Sun, C. Zou, Y. Fang and W. Sun: methodology, investigation and writing. S. He, Y. Liu, and J. Zhang: visualization, investigation, and formal analysis. Y. Zhu and J. Wang: funding acquisition and writing – review & editing.

Conflicts of interest

There are no conflicts to declare.

Acknowledgements

Notes and references

1 P. De Luna, C. Hahn, D. Higgins, S. A. Jaffer, T. F. Jaramillo and E. H. Sargent, What would it take for renewably powered electrosynthesis to displace petrochemical processes?, *Science*, 2019, **364**, eaav3506.

2 Z. Y. Sun, T. Ma, H. C. Tao, Q. Fan and B. X. Han, Fundamentals and challenges of electrochemical CO$_2$ reduction using two-dimensional materials, *Chem*, 2017, **3**, 560–587.

3 L. Zhang, Z. J. Zhao and J. L. Gong, Nanostructured materials for heterogeneous electrocatalytic CO$_2$ reduction and their related reaction mechanisms, *Angew. Chem., Int. Ed.*, 2017, **56**, 11326–11353.

4 S. Navarro-Jaen, M. Virginie, J. Bonin, M. Robert, R. Wojcieszak and A. Y. Khodakov, Highlights and challenges in the selective reduction of carbon dioxide to methanol, *Nat. Rev. Chem.*, 2021, **5**, 564–579.

5 D. F. Gao, R. M. Aran-Ais, H. S. Jeon and B. Roldan, Cuenya, Rational catalyst and electrolyte design for CO$_2$ electroreduction towards multicarbon products, *Nat. Catal.*, 2019, **2**, 198–210.

6 W. C. Ma, X. Y. He, W. Wang, S. J. Xie, Q. H. Zhang and Y. Wang, Electrocatalytic reduction of CO$_2$ and CO to multicarbon compounds over Cu-based catalysts, *Chem. Soc. Rev.*, 2021, **50**, 12897–12914.

7 G. X. Wang, J. X. Chen, Y. C. Ding, P. W. Cai, L. C. Yi, Y. Li, C. Y. Tu, Y. Hou, Z. H. Wen and L. M. Dai, Electrocatalysis for CO$_2$ conversion: from fundamentals to value-added products, *Chem. Soc. Rev.*, 2021, **50**, 4993–5061.

8 J. L. Yu, J. Wang, Y. B. Ma, J. W. Zhou, Y. H. Wang, P. Y. Lu, J. W. Yin, R. Q. Ye, Z. L. Zhu and Z. X. Fan, Recent progresses in electrochemical carbon dioxide reduction on copper-based catalysts toward multicarbon products, *Adv. Funct. Mater.*, 2021, **31**, 2102151.

9 Y. Gong, J. Pan, L. Zhang, X. Wang, S. Song and H. Zhang, Metal-organic frameworks-derived Indium clusters/carbon nanocomposites for efficient CO$_2$ electroreduction, *Chem. Res. Chin. Univ.*, 2022, **38**, 1287–1291.

10 H. Shin, K. U. Hansen and F. Jiao, Techno-economic assessment of low-temperature carbon dioxide electrolysis, *Nat. Sustain.*, 2021, **4**, 911–919.

11 R. S. Weber, The challenges of electrolytic valorization of carbon dioxide, *Nat. Sustain.*, 2021, **4**, 839–840.

12 R. I. Masel, Z. C. Liu, H. Z. Yang, J. J. Kaczur, D. Carrillo, S. X. Ren, D. Salvatore and C. P. Berlinguette, An industrial perspective on catalysts for low-temperature CO_2 electrolysis, *Nat. Nanotechnol.*, 2021, **16**, 118–128.

13 P. Zhu and H. T. Wang, High-purity and high-concentration liquid fuels through CO_2 electroreduction, *Nat. Catal.*, 2021, **4**, 943–951.

14 C. Xia, P. Zhu, Q. Jiang, Y. Pan, W. T. Liang, E. Stavitsk, H. N. Alshareef and H. T. Wang, Continuous production of pure liquid fuel solutions *via* electrocatalytic CO_2 reduction using solid-electrolyte devices, *Nat. Energy*, 2019, **4**, 776–785.

15 K. Sordakis, C. H. Tang, L. K. Vogt, H. Junge, P. J. Dyson, M. Beller and G. Laurenczy, Homogeneous catalysis for sustainable hydrogen storage in formic acid and alcohols, *Chem. Rev.*, 2018, **118**, 372–433.

16 S. Nitopi, E. Bertheussen, S. B. Scott, X. Y. Liu, A. K. Engstfeld, S. Horch, B. Seger, I. E. L. Stephens, K. Chan, C. Hahn, J. K. Norskov, T. F. Jaramillo and I. Chorkendorff, Progress and perspectives of electrochemical CO_2 reduction on copper in aqueous electrolyte, *Chem. Rev.*, 2019, **119**, 7610–7672.

17 Y. Hori, H. Wakebe, T. Tsukamoto and O. Koga, Electrocatalytic process of CO selectivity in electrochemical reduction of CO_2 at metal-electrodes in aqueous-media, *Electrochim. Acta*, 1994, **39**, 1833–1839.

18 Y. Du, X. Zheng, Y. Xue and Y. Li, Bismuth/Graphdiyne heterostructure for electrocatalytic conversion of CO_2 to formate, *Chem. Res. Chin. Univ.*, 2022, **38**, 1380–1386.

19 F. Yang, A. O. Elnabawy, R. Schimmenti, P. Song, J. W. Wang, Z. Q. Peng, S. Yao, R. P. Deng, S. Y. Song, Y. Lin, M. Mavrikakis and W. L. Xu, Bismuthene for highly efficient carbon dioxide electroreduction reaction, *Nat. Commun.*, 2020, **11**, 1088.

20 D. Z. Yao, C. Tang, A. Vasileff, X. Zhi, Y. Jiao and S. Z. Qiao, The controllable reconstruction of Bi-MOFs for electrochemical CO_2 reduction through electrolyte and potential mediation, *Angew. Chem., Int. Ed.*, 2021, **60**, 18178–18184.

21 S. S. He, F. L. Ni, Y. J. Ji, L. E. Wang, Y. Z. Wen, H. P. Bai, G. J. Liu, Y. Zhang, Y. Y. Li, B. Zhang and H. S. Peng, The p-orbital delocalization of main-group metals to boost CO_2 electroreduction, *Angew. Chem., Int. Ed.*, 2018, **57**, 16114–16119.

22 Y. L. Yuan, Q. Y. Wang, Y. Qiao, X. L. Chen, Z. L. Yang, W. C. Lai, T. W. Chen, G. H. Zhang, H. G. Duan, M. Liu and H. W. Huang, In situ structural reconstruction to generate the active sites for CO_2 electroreduction on bismuth ultrathin nanosheets, *Adv. Energy Mater.*, 2022, **12**, 2200970.

23 F. P. Pan and Y. Yang, Designing CO_2 reduction electrode materials by morphology and interface engineering, *Energy Environ. Sci.*, 2020, **13**, 2275–2309.

24 F. P. G. de Arquer, O. S. Bushuyev, P. De Luna, C. T. Dinh, A. Seifitokaldani, M. I. Saidaminov, C. S. Tan, L. N. Quan, A. Proppe, M. G. Kibria, S. O. Kelley, D. Sinton and E. H. Sargent, 2D metal oxyhalide-derived catalysts for efficient CO_2 electroreduction, *Adv. Mater.*, 2018, **30**, 1802858.

25 Z. P. Chen, K. W. Mou, X. H. Wang and L. C. Liu, Nitrogen-doped graphene quantum dots enhance the activity of Bi_2O_3 nanosheets for electrochemical reduction of CO_2 in a wide negative potential region, *Angew. Chem., Int. Ed.*, 2018, **57**, 12790–12794.

26 S. B. Liu, X. F. Lu, J. Xiao, X. Wang and X. W. Lou, Bi_2O_3 nanosheets grown on multi-channel carbon matrix to catalyze efficient CO_2 electroreduction to HCOOH, *Angew. Chem., Int. Ed.*, 2019, **58**, 13828–13833.

27 H. Yang, N. Han, J. Deng, J. H. Wu, Y. Wang, Y. P. Hu, P. Ding, Y. F. Li, Y. G. Li and J. Lu, Selective CO_2 reduction on 2D mesoporous Bi nanosheets, *Adv. Energy Mater.*, 2018, **8**, 1801536.

28 P. L. Deng, F. Yang, Z. T. Wang, S. H. Chen, Y. Z. Zhou, S. Zaman and B. Y. Xia, Metal-organic framework-derived carbon nanorods encapsulating bismuth oxides for rapid and selective CO_2 electroreduction to formate, *Angew. Chem., Int. Ed.*, 2020, **59**, 10807–10813.

29 L. Lin, X. Y. He, X. G. Zhang, W. C. Ma, B. Zhang, D. Y. Wei, S. J. Xie, Q. H. Zhang, X. D. Yi and Y. Wang, A nanocomposite of bismuth clusters and $Bi_2O_2CO_3$ sheets for highly efficient electrocatalytic reduction of CO_2 to formate, *Angew. Chem., Int. Ed.*, 2022, **62**, e202214959.

30 Y. L. Shi, C. F. Wen, X. F. Wu, J. Y. Zhao, F. X. Mao, P. F. Liu and H. G. Yang, In situ reconstruction of vegetable sponge-like Bi_2O_3 for efficient CO_2 electroreduction to formate, *Mater. Chem. Front.*, 2022, **6**, 1091–1097.

31 B. Wulan, L. Zhao, D. Tan, X. Cao, J. Ma and J. Zhang, Electrochemically driven interfacial transformation for high performing solar to fuel electrocatalytic conversion, *Adv. Energy Mater.*, 2022, **12**, 2103960.

32 Y. X. Duan, Y. T. Zhou, Z. Yu, D. X. Liu, Z. Wen, J. M. Yan and Q. Jiang, Boosting production of HCOOH from CO_2 electroreduction *via* Bi/CeO_x, *Angew. Chem., Int. Ed.*, 2021, **60**, 8798–8802.

33 L. Li, A. Ozden, S. Y. Guo, F. P. G. de Arquer, C. H. Wang, M. Z. Zhang, J. Zhang, H. Y. Jiang, W. Wang, H. Dong, D. Sinton, E. H. Sargent and M. Zhong, Stable, active CO_2 reduction to formate *via* redox-modulated stabilization of active sites, *Nat. Commun.*, 2021, **12**, 5223.

34 B. H. Ren, G. B. Wen, R. Gao, D. Luo, Z. Zhang, W. B. Qiu, Q. Y. Ma, X. Wang, Y. Cui, L. Ricardez-Sandoval, A. P. Yu and Z. W. Chen, Nano-crumples induced Sn–Bi bimetallic interface pattern with moderate electron bank for highly efficient CO_2 electroreduction, *Nat. Commun.*, 2022, **13**, 2486.

35 J. H. Zhou, K. Yuan, L. Zhou, Y. Guo, M. Y. Luo, X. Y. Guo, Q. Y. Meng and Y. W. Zhang, Boosting electrochemical reduction of CO_2 at a low overpotential by amorphous Ag–Bi–S–O decorated Bi^0 nanocrystals, *Angew. Chem., Int. Ed.*, 2019, **58**, 14197–14201.

36 B. W. Liu, Y. Xie, X. L. Wang, C. Gao, Z. M. Chen, J. Wu, H. Y. Meng, Z. C. Song, S. C. Du and Z. Y. Ren, Copper-triggered delocalization of bismuth p-orbital favours high-throughput CO2 electroreduction, *Appl. Catal., B*, 2022, **301**, 120781.

37 Y. T. Wang, L. Cheng, Y. H. Zhu, J. Z. Liu, C. Q. Xiao, R. Z. Chen, L. Zhang, Y. H. Li and C. Z. Li, Tunable selectivity on copper-bismuth bimetallic aerogels for electrochemical CO_2 reduction, *Appl. Catal., B*, 2022, **317**, 121650.

38 H. D. Shen, Y. K. Zhao, L. Zhang, Y. He, S. W. Yang, T. S. Wang, Y. L. Cao, Y. Guo, Q. Y. Zhang and H. P. Zhang, In-situ constructuring of copper-doped bismuth catalyst for highly efficient CO_2 electrolysis to formate in ampere-level, *Adv. Energy Mater.*, 2022, **13**, 2202818.

39 A. G. A. Mohamed, E. Zhou, Z. Zeng, J. Xie, D. Gao and Y. Wang, Asymmetric oxo-bridged ZnPb bimetallic electrocatalysis boosting CO_2 to HCOOH reduction, *Adv. Sci.*, 2022, **9**, e2104138.

40 T. Zheng, C. Liu, C. Guo, M. Zhang, X. Li, Q. Jiang, W. Xue, H. Li, A. Li, C. W. Pao, J. Xiao, C. Xia and J. Zeng, Copper-catalysed exclusive CO_2 to pure formic acid conversion *via* single-atom alloying, *Nat. Nanotechnol.*, 2021, **16**, 1386–1393.

41 Y. L. Yu, S. L. Huang, Y. Gu, S. Yan, Z. J. Lan, W. J. Zheng and Y. A. Cao, Study of PbBiO₂X (X = Cl, Br and I) square nanoplates with efficient visible photocatalytic performance, *Appl. Surf. Sci.*, 2018, **428**, 844–850.

42 M. L. Guan, C. Xiao, J. Zhang, S. J. Fan, R. An, Q. M. Cheng, J. F. Xie, M. Zhou, B. J. Ye and Y. Xie, Vacancy associates promoting solar-driven photocatalytic activity of ultrathin bismuth oxychloride nanosheets, *J. Am. Chem. Soc.*, 2013, **135**, 10411–10417.

43 Y. Zhou, P. Yan, J. Jia, S. Zhang, X. Zheng, L. Zhang, B. Zhang, J. Chen, W. Hao, G. Chen, Q. Xu and B. Han, Supercritical CO_2-constructed intralayer $[Bi_2O_2]^{2+}$ structural distortion for enhanced CO_2 electroreduction, *J. Mater. Chem. A*, 2020, **8**, 13320–13327.

44 Y. Yu, S. Huang, Y. Gu, S. Yan, Z. Lan, W. Zheng and Y. Cao, Study of PbBiO₂X (X = Cl, Br and I) square nanoplates with efficient visible photocatalytic performance, *Appl. Surf. Sci.*, 2018, **428**, 844–850.

45 W. Zhong, D. Li, S. Jin, W. Wang and X. Yang, Synthesis and structure of BiPbO₂Cl nanosheet with enhanced visible light photocatalytic activity, *Appl. Surf. Sci.*, 2015, **356**, 1341–1348.

46 X. Z. Feng, R. J. Zheng, C. Y. Gao, W. F. Wei, J. G. L. Peng, R. H. Wang, S. H. Yang, W. S. Zou, X. Y. Wu, Y. F. Ji and H. Chen, Unlocking bimetallic active sites *via* a desalination strategy for photocatalytic reduction of atmospheric carbon dioxide, *Nat. Commun.*, 2022, **13**, 2146.

47 X. Fu, J. Wang, X. Hu, K. He, Q. Tu, Q. Yue and Y. Kang, Scalable chemical interface confinement reduction BiOBr to bismuth porous nanosheets for electroreduction of carbon dioxide to liquid fuel, *Adv. Funct. Mater.*, 2022, **32**, 2107182.